Surface Wave Effects on the Translation of Wind Stress across the Air–Sea Interface in a Fetch-Limited, Coastal Embayment

ALEXANDER W. FISHER

University of Maryland Center for Environmental Science, Horn Point Laboratory, Cambridge, Maryland, and Department of Geography, University of California, Santa Barbara, Santa Barbara, California

LAWRENCE P. SANFORD

University of Maryland Center for Environmental Science, Horn Point Laboratory, Cambridge, Maryland

MALCOLM E. SCULLY

Applied Ocean Physics and Engineering, Woods Hole Oceanographic Institution, Woods Hole, Massachusetts

STEVEN E. SUTTLES

University of Maryland Center for Environmental Science, Horn Point Laboratory, Cambridge, Maryland

(Manuscript received 15 June 2016, in final form 27 March 2017)

ABSTRACT

The role of surface gravity waves in structuring the air–sea momentum flux is examined in the middle reaches of Chesapeake Bay. Observed wave spectra showed that wave direction in Chesapeake Bay is strongly correlated with basin geometry. Waves preferentially developed in the direction of maximum fetch, suggesting that dominant wave frequencies may be commonly and persistently misaligned with local wind forcing. Direct observations from an ultrasonic anemometer and vertical array of ADVs show that the magnitude and direction of stress changed across the air–sea interface, suggesting that a stress divergence occurred at or near the water surface. Using a numerical wave model in combination with direct flux measurements, the air–sea momentum flux was partitioned between the surface wave field and the mean flow. Results indicate that the surface wave field can store or release a significant fraction of the total momentum flux depending on the direction of the wind. When wind blew across dominant fetch axes, the generation of short gravity waves stored as much as 40% of the total wind stress. Accounting for the storage of momentum in the surface wave field closed the air–sea momentum budget. Agreement between the direction of Lagrangian shear and the direction of the stress vector in the mixed surface layer suggests that the observed directional difference was due to the combined effect of breaking waves producing downward sweeps of momentum in the direction of wave propagation and the straining of that vorticity field in a manner similar to Langmuir turbulence.

1. Introduction

Surface gravity waves act as dynamic roughness elements at the water surface and play an important role in regulating air–sea momentum and energy fluxes through increased drag at the air–sea interface associated with wave generation (Janssen 1989), energy transfer beneath breaking waves (Craig and Banner 1994; Terray et al. 1996), and Langmuir turbulence (Craik and Leibovich 1976; Leibovich 1983). Growing recognition that material exchange in estuaries can be dominated by wind-driven circulation (Sanford and Boicourt 1990; Chen et al. 2009; Scully 2010a; Scully 2013) has prompted numerous investigations into the momentum balances of wind-driven flows in estuaries (Geyer 1997; Chen and Sanford 2009; Scully 2010b; Li and Li 2011; Li and Li 2012). Very few of these studies, however, have accounted for surface gravity waves in the energy and momentum budgets of the mean flow. Fetch limitation in coastal environments often results in wind seas that never reach full saturation, suggesting that the surface

University of Maryland Center for Environmental Science Contribution Number 5355.

Corresponding author: Alexander Fisher, awfisher@ucsb.edu

DOI: 10.1175/JPO-D-16-0146.1

wave field may also play an important role in the local air–sea momentum budget in coastal environments.

We present an analysis of the air–sea momentum flux building on the observations of Langmuir turbulence and momentum transfer beneath breaking waves presented in Scully et al. (2015) and Scully et al. (2016), respectively. Specifically, the focus of this manuscript is to investigate the effects of surface gravity waves in the translation of stress across the air–sea interface. As Scully et al. (2016) showed, using the same dataset presented here, direct measurements of the atmospheric surface wind stress and the momentum flux vector observed in the surface layer of the estuary suggest that the local air–sea momentum budget is not closed. Furthermore, Scully et al. (2016) hypothesized that a stress divergence occurs very near the air–sea interface. Using a combination of direct observations and numerical simulations, we investigate the effects of surface gravity waves on the translation of wind stress across the air–sea interface and into the surface layer of the estuary.

2. Background

The evolution of wind stress at the water surface and its subsequent translation into the mixed surface layer is mediated by the presence of surface gravity waves and their interaction with mean and turbulent flows. These effects can be expressed as a modulation of stress at the water surface principally through wind–wave interactions and the modification of vertical mixing regimes through enhanced dissipation (e.g., wave breaking) and/or a restructuring of boundary layer transport through coherent wave-driven turbulence (e.g., Langmuir turbulence).

a. *Wind-wave effects in the atmospheric surface boundary layer*

Numerous studies have shown that wind stress measurements exhibit a strong wave dependency in which the aerodynamic drag of young seas is higher than that of mature seas (Kitaigorodskii 1973; Donelan 1982; Geernaert et al. 1986; Smith et al. 1992; Johnson and Vested 1992; Johnson et al. 1998; Komen et al. 1998; Oost et al. 2002; Drennan et al. 2003; Edson et al. 2013). Even for old wind seas, the drag is larger than that expected for a smooth plate (Donelan 1982); however, long gravity waves support little of this wave-induced stress because their phase speed is typically on the same order as the wind speed. Therefore, the aerodynamic drag must primarily be due to the momentum sink associated with the generation of high-frequency, short gravity waves (Janssen 1989). The Charnock parameter is used to parameterize this effect by partitioning the roughness parameter into a smooth and rough component due to surface waves (Charnock 1955). This formulation yields an approximately linear relationship between the drag coefficient and wind speed when the Charnock parameter is taken as constant. Numerous studies have accounted for sea state within this parameter by using a wave age (C_p/u_* or C_p/U_{10}) formulation of the drag coefficient or the Charnock parameter (Geernaert et al. 1986; Lin et al. 2002; Edson et al. 2013; Fisher et al. 2015). In coastal environments, fetch limitation can result in high degrees of spatial variability in surface wind stress due to a combination of variable surface winds and waves, which can result in significant spatial and temporal variations in the drag coefficient (Fisher et al. 2015).

b. *Stress partitioning*

Partitioning the air–sea momentum flux between the surface wave field and the mean flow may offer insights into the role surface gravity waves play in the local air–sea momentum budget. Independent of direct wind stress, waves can drive significant flows in nearshore environments through gradients in radiation stress (Longuet-Higgins 1970) and mass transport resulting from Stokes drift (Monismith and Fong 2004). The effects of surface gravity waves on the mean flow are commonly examined using radiation stress theory (Longuet-Higgins and Stewart 1960, 1964); however, because radiation stresses are formulated in the momentum balance of a total flow that includes the mean current and the surface wave field, radiation stress does not describe the partitioning of momentum between the wave field and the mean flow. To investigate the momentum transfer between waves and the mean flow, we partition the air–sea momentum flux following the interaction stress theory developed by Hasselmann (1971).

A full derivation of the horizontal momentum equations that accounts for a complete flow including surface waves is described in Hasselmann (1971) for a nonrotating frame and Ardhuin et al. (2004) for a rotating frame. By time averaging these equations, the interactions of the mean flow with the surface wave field arise from the nonlinear terms and the pressure field. This ''interaction stress'' tensor is defined as the sum of the Reynolds stress and the wave-induced mean pressure (Hasselmann 1971):

$$\tau_{ij}^{\text{int}} = -\rho_w(\overline{u_i' u_j'} + p^w \delta_{ij}), \tag{1}$$

where ρ_w is the density of seawater, u' is the fluctuating velocity, and p^w is the nonhydrostatic pressure associated with wave motion within a wavy surface layer that exists between the mean and fluctuating component of the free surface $\zeta(x, y, t)$. Indices i and j refer to Eulerian

coordinates x, y, and z. Prime values denote rapid oscillations associated with a wavy free surface. The derivation of Eq. (1) does not make any assumptions regarding the dynamics of the fluctuating field u' and ζ' other than an assumption of the analytical continuation of fields for $\zeta' < 0$ to the mean free surface (Hasselmann 1971). Therefore, the interaction stress is a robust term that applies to interactions involving waves and turbulence that are modified by strongly nonlinear processes (Hasselmann 1971; Ardhuin et al. 2004).

In the following equations, we adopt the notation of Hasselmann (1971) in which dummy indices α and β correspond to horizontal components. Separation of the momentum flux between waves and the mean flow can be examined by partitioning the vertically integrated momentum M balance between the mean flow (superscript m) and a wavy surface layer (superscript w) constrained between the mean free surface and the instantaneous free surface:

$$\begin{aligned}\overline{M_\alpha} &= \rho_w \overline{\int_{-h}^{\zeta} u_\alpha \, dz} = \rho_w \overline{\int_{-h}^{\overline{\zeta}} u_\alpha \, dz} + \rho_w \overline{\int_{\overline{\zeta}}^{\overline{\zeta}+\zeta'} u_\alpha \, dz} \\ &= \overline{M_\alpha^m} + \overline{M_\alpha^w}, \end{aligned} \tag{2}$$

where h is depth and u is velocity. Overbars denote averages over several wave periods. Furthermore, we note that wave energy spectral density can be used in the formulation of wave momentum (Ardhuin et al. 2004):

$$\overline{M^w} = \rho_w g \int \frac{kF(k)}{|k|C} \, dk, \tag{3}$$

where $F(k)$ is the wave energy spectral density as a function of the wavenumber vector k, and C is the wave phase speed.

The evolution of the depth-integrated, time-averaged momentum of the horizontal α component of the total flow can be expressed as (Ardhuin et al. 2004)

$$\begin{aligned}\underbrace{\frac{\partial \overline{M_\alpha}}{\partial t}}_{\text{(i)}} &= \Bigg[\underbrace{\frac{\partial T^m_{\alpha\beta}}{\partial x_\beta}}_{\text{(ii)}} + \underbrace{\overline{p^a} \frac{\partial \overline{\zeta}}{\partial x_\alpha}}_{\text{(iii)}} + \underbrace{(p^m + gh)_{-h} \frac{\partial h}{\partial x_\alpha}}_{\text{(iv)}} \\ &\quad + \underbrace{fM^m_\beta (1 - \delta_{\alpha\beta})}_{\text{(v)}} + \underbrace{\tau^{\text{air}}_\alpha}_{\text{(vi)}} - \underbrace{\tau^{\text{bot}}_\alpha}_{\text{(vii)}} \Bigg] + \underbrace{\frac{\partial T^{\text{rad}}_{\alpha\beta}}{\partial x_\beta}}_{\text{(viii)}} \\ &\quad + \underbrace{p^w_{-h} \frac{\partial h}{\partial x_\alpha}}_{\text{(ix)}} + \underbrace{fM^w_\beta (1 - \delta_{\alpha\beta})}_{\text{(x)}}, \end{aligned} \tag{4}$$

where the terms on the RHS are (ii) horizontal divergence of depth-integrated total mean stress, (iii) pressure gradient force, (iv) mean bottom pressure including hydrostatic pressure, (v) Coriolis force of mean flow, the (vi) surface and (vii) bottom shear stresses, (viii) the horizontal divergence of radiation stress tensor, and the (ix) wave-added pressure term and (x) wave-added Coriolis force. Note that τ represents true stresses ($\mathrm{N\,m^{-2}}$), whereas T terms represent depth-integrated stresses that have units of the total force per unit width ($\mathrm{N\,m^{-1}}$). The overall momentum equation is the result of depth integrating the equations of motion and averaging over several wave periods, evoking appropriate boundary conditions.

Integrating the equations of motion from $z = -h$ to $\overline{\zeta}$ yields the mean flow momentum equation [Ardhuin et al. 2004, their Eqs. (15), (16)]:

$$\begin{aligned}\underbrace{\frac{\partial \overline{M^m_\alpha}}{\partial t}}_{\text{(i)}} &= \Bigg[\underbrace{\frac{\partial T^m_{\alpha\beta}}{\partial x_\beta}}_{\text{(ii)}} + \underbrace{\overline{p^a} \frac{\partial \overline{\zeta}}{\partial x_\alpha}}_{\text{(iii)}} + \underbrace{(p^m + gh)_{-h} \frac{\partial h}{\partial x_\alpha}}_{\text{(iv)}} \\ &\quad + \underbrace{fM^m_\beta (1 - \delta_{\alpha\beta})}_{\text{(v)}} + \underbrace{\tau^{\text{air}}_\alpha}_{\text{(vi)}} - \underbrace{\tau^{\text{bot}}_\alpha}_{\text{(vii)}} \Bigg] + \underbrace{\frac{\partial T^{\text{int}}_{\alpha\beta}}{\partial x_\beta}}_{\text{(viii)}} \\ &\quad + \underbrace{(\tau^{\text{air}}_\alpha - \tau^{\text{int}}_\alpha)}_{\text{(ix)}} + \underbrace{p^w_{-h} \frac{\partial h}{\partial x_\alpha}}_{\text{(x)}} + \underbrace{fM^w_\beta (1 - \delta_{\alpha\beta})}_{\text{(xi)}}. \end{aligned} \tag{5}$$

The bracketed terms on the right-hand side (the second through seventh terms) of the equation are the usual terms in the horizontal momentum equation of the mean flow including the effects of rotation. The eighth term is the horizontal divergence of the interaction stress tensor:

$$T^{\text{int}}_{\alpha\beta} = \int_{-h}^{\overline{\zeta}} \tau^{\text{int}}_{\alpha\beta} \, dz. \tag{6}$$

It is informative to explore the wave contributions to the depth-integrated interaction stress tensor in Eq. (6) by assuming a quasi-linear wave field. Using this simplified approach, Ardhuin et al. (2004) showed that the wave component of the depth-integrated interaction stress can be expressed as

$$T^{\text{int}}_{\alpha\beta} = \rho_w g \int F(k) \left\{ \left[1 - \frac{C_g(k)}{C(k)} \right] \delta_{\alpha\beta} - \frac{C_g(k)}{C(k)} \frac{k_\alpha k_\beta}{k^2} \right\} dk, \tag{7}$$

where C_g is the group speed. Thus, the depth-integrated wave component of the interaction stress is equal to the

depth-integrated pressure added by surface waves (term 1 in the braces) and the nonisotropic wave momentum advected by waves (term 2 in the braces; Ardhuin et al. 2004).

The difference between τ^{air} and τ^{int} represents the portion of the air–sea momentum flux that is stored in (positive) or released by (negative) the surface wave field to the mean flow (Ardhuin et al. 2004). For wind and waves that are aligned, this fraction decreases as a function of wave age from roughly 10% for very young seas to near zero for a mature wind sea (Ardhuin et al. 2004) consistent with the findings of Mitsuyasu (1985). Analysis of momentum storage in a misaligned wave field, however, has not been addressed in the literature to our knowledge.

The momentum evolution equation of the wave surface layer can be determined by subtracting Eq. (5) from Eq. (4):

$$\frac{\partial M^w_\alpha}{\partial t} - \nabla \cdot T^{\text{sl}}_{\alpha\beta} = \tau^{\text{air}}_\alpha - \tau^{\text{int}}_\alpha , \tag{8}$$

where $T^{\text{sl}}_{\alpha\beta}$ is the depth-integrated stress acting on the wavy surface layer defined as

$$T^{\text{sl}}_{\alpha\beta} = -\overline{\int_{\bar\zeta}^{\bar\zeta+\zeta'} (p\delta_{\alpha\beta} + \rho_w u'_\alpha u'_\beta)\, dx_3} . \tag{9}$$

A conceptual diagram illustrating the partitioning of the momentum budget between the mean flow and the surface wave field is shown in Fig. 1. The interaction stress represents the shear stress acting on the mean flow or the shear stress acting at the mean free surface. The radiation stress, therefore, can be expressed as the sum of the average stress acting on the wavy surface layer and the interaction stress.

c. *Wave-enhanced turbulent mixing*

The effects of surface gravity waves on mixing and material transport within the water column can take many forms and usually result in an enhancement of vertical exchange relative to wall-bounded shear flows. Focusing on the ocean surface mixed layer, we will restrict our discussion to whitecapping dissipation, mixing due to breaking waves (Scully et al. 2016), and Langmuir turbulence (Scully et al. 2015). Wave breaking and Langmuir turbulence are strongly coupled, so the distinction between the two processes may not be informative or meaningful in a shallow estuarine environment where coherent cells are modified by tidal shear, strong vertical density gradients, and bottom boundary layer dynamics. For simplicity, we refer to the sum of the latter two terms as wave-controlled coherent turbulence.

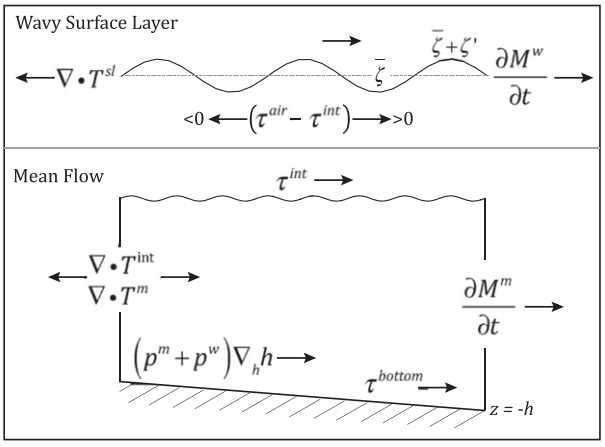

FIG. 1. Conceptual diagram of partitioning the air–sea momentum flux between the surface wave field and the mean flow using interaction stress theory. The wave momentum is contained in a wavy surface layer between the mean free surface $\bar\zeta$ and the instantaneous free surface $\bar\zeta + \zeta'$. The fraction of momentum stored in or released by the surface wave field can be expressed as the difference between the wind stress and the interaction stress. The interaction stress then represents the surface shear stress acting on a mean flow that accounts for the effects of a wavy free surface. A similar diagram is shown in Ardhuin et al. (2004).

Wave breaking is a primary mechanism through which mechanical energy and momentum are transferred from the atmosphere to the mean flow (Melville 1996). Rapp and Melville (1990) suggested that the momentum flux associated with breaking waves constitutes a majority of the air–sea flux. Wave breaking in deep water is the result of wind–wave, wave–wave, and wave–current interactions (Melville 1996). Measured distributions of breaking rate show a peak at a phase speed approximately half that of the spectral peak with dissipation of high-frequency, short waves composing a significant fraction of the total breaking rate (Gemmrich et al. 2008; Thomson et al. 2009; Schwendeman et al. 2014). Schwendeman et al. (2014) also noted that a regime shift occurs in young wind seas where large whitecaps replace, not add to, small-scale breakers as forcing becomes stronger. Furthermore, field observations of the dissipation of turbulent kinetic energy (TKE) beneath surface gravity waves exceed wall-bounded shear flow scaling (Kitaigorodskii et al. 1983; Agrawal et al. 1992; Drennan et al. 1992; Terray et al. 1996; Drennan et al. 1996,; Gemmrich and Farmer 1999,; Gemmrich 2010; Scully et al. 2016).

Coherent wave-driven turbulence can enhance the transport of momentum and energy beneath breaking waves into the oceanic surface layer through a combination of u-shaped vortices generated near the surface by whitecapping waves (Melville et al. 2002; Scully et al.

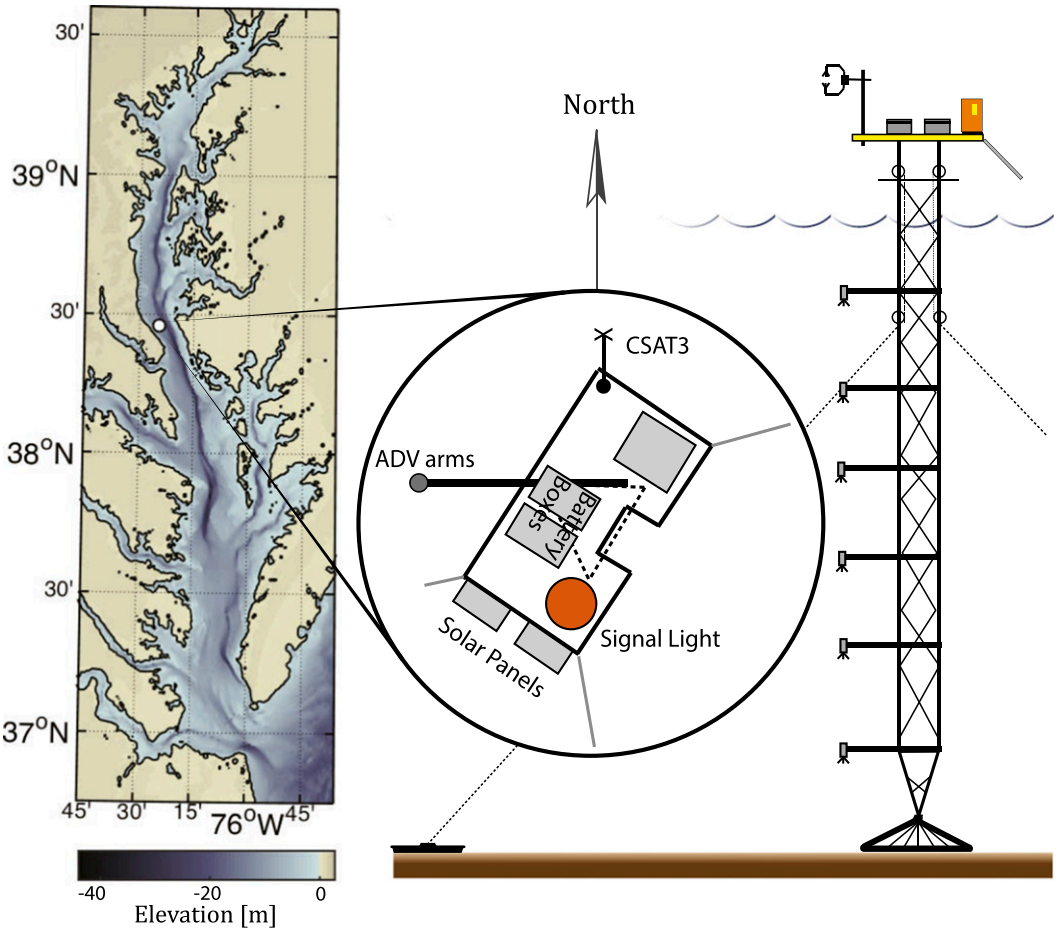

FIG. 2. Map and tower schematic. Inset diagram shows the orientation of the tower, ultrasonic anemometer, and ADVs. Tower schematic at right shows vertical array structure.

2016) and larger-scale Langmuir circulations that can occupy the full depth of the surface mixed layer (Plueddemann and Weller 1999; D'Asaro 2001; Gerbi et al. 2008; Scully et al. 2015). It is generally accepted that Langmuir turbulence arises from a straining of the vorticity field generated beneath breaking waves by Stokes drift (Craik 1977; Leibovich 1977) and can significantly increase turbulent length and velocity scales relative to a wall-bounded shear flow (McWilliams et al. 1997; Li et al. 2005; Harcourt and D'Asaro 2008). Additionally, wave-controlled coherent turbulence may play an important role in entrainment at the base of the surface mixed layer directly or indirectly by enhancing Kelvin–Helmholtz billowing through a concentration of shear near the pycnocline (Li and Garrett 1997; Kukulka et al. 2010).

3. Methods

The centerpiece of a field deployment that included instrumented surface buoys, bottom landers, and towed instrument surveys was a turbulence tower deployed on a western shoal of the middle reaches of Chesapeake Bay (38 27′39″, 76 24′44″) in a 14-m-deep region of slowly varying bathymetry. It was held vertically rigid using four guy-wires, which were secured to the top of the 16-m tower and anchored to 1000-lb railcar wheels. The tower was deployed on 18 September 2013 and recovered on 29 October 2013. A schematic of the tower and map of the deployment site are shown in Fig. 2.

High-resolution velocity data used in the estimation of momentum fluxes were recorded using a vertical array of Nortek vector acoustic Doppler velocimeters (ADVs) in the water column and an ultrasonic anemometer deployed on an aerial platform atop the tower. The downward-looking ADV heads were mounted to 1-m aluminum arms attached to the tower ~2 m apart in the vertical, starting approximately 1.5 m below the mean water surface. The aluminum arms were oriented due west. The ADVs recorded three-dimensional

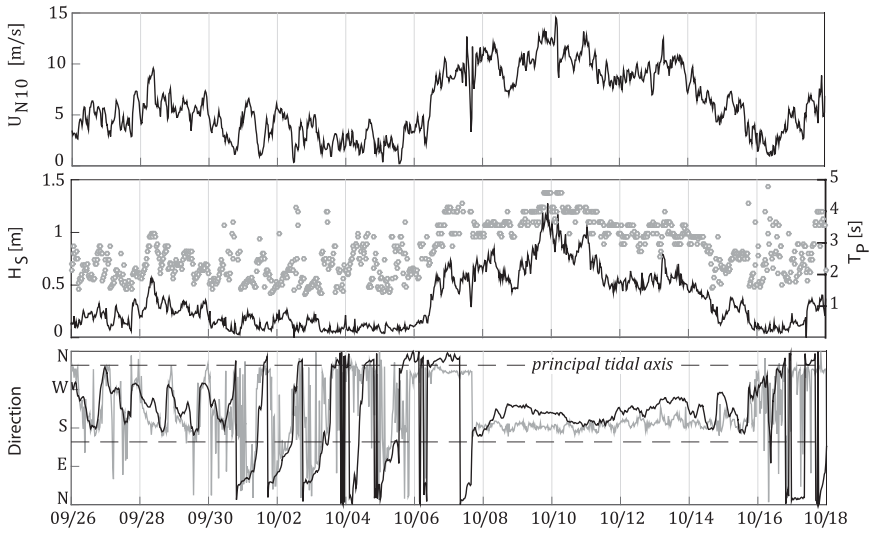

FIG. 3. Wind and wave conditions at tower during the deployment. (top) The 10-m neutral wind speed. (middle) Significant wave height (black) and peak period (gray dots). (bottom) Wind (black) and wave (gray) direction in oceanographic convention. The principal tidal axes are also shown as dashed black lines.

velocity and pressure data at 32 Hz in 28-min bursts centered 30 min apart.

Direct measurements of air–sea momentum and sensible heat fluxes were collected by a Campbell Scientific CSAT3 ultrasonic anemometer with fine-wire thermocouple deployed on top of the tower. The anemometer was oriented due north and had a sampling volume elevation of ~2.82 m MSL. The tidal range at the tower site was approximately 0.5 m, so the elevation of the anemometer ranged from ~2.3 to ~3.3 m above the water surface. The system sampled the 3D velocity field and air temperature at 10 Hz continuously. The anemometer was deployed on 25 September 2013 and recovered on 28 October 2013.

a. Data analysis

The analysis period was constrained to three weeks spanning 25 September 2013 to 18 October 2013 due to the exhaustion of ADV batteries at the end of the deployment. Additionally, periods of tower-induced flow distortion were omitted when the mean current was coming from 70° [degrees true (°T)] to 130°T and when the winds blew from 170°T to 250°T.

Directional wave spectra were calculated from the uppermost ADV data ($z = -1.7$ m) using the pressure and horizontal velocity (PUV) method based on linear wavy theory and the Directional Wave Spectra (DIWASP) MATLAB toolkit (Johnson 2002). The 32-Hz pressure and 3D velocity data from the ADV were resampled at 8 Hz, and a 1024-s segment of each burst, starting with the ninth sample in the resampled burst, was used for each wave burst. Resampling was performed using MATLAB's resample function, in which the data are low-pass filtered using a Kaiser window. Additionally, the pressure signal was corrected for variations in atmospheric pressure using barometric pressure data from the Cove Point NOS station (~6.9 km southeast of tower site) and low-pass filtered using a second-order Butterworth filter with a 1-Hz cutoff. The total energy level in each frequency was set using the corrected pressure signal. An f^{-4} tail was fit to observational spectra due to an inability of resolving wave frequencies above 0.6 Hz due to the depth of the pressure sensor (Jones and Monismith 2007). Doppler shifting by the mean currents was accounted for by adjusting the frequency vector of observed wave spectra using linear wave theory.

A summary of tower conditions observed during the deployment is presented in Fig. 3. The deployment was dominated by a 10-day nor'easter that was recorded between 6 and 16 October 2013. The event was characterized by winds blowing from northeast to north at an average wind speed of 7 m s^{-1}. Wind stress peaked at 0.31 Pa, with an event average of 0.13 Pa. The event generated a surface wave field that had a significant wave height of ~1 m and typical peak wave period of 4 s. Tidal velocities were aligned with the central channel at 150°T. Note that wave direction and period data for times when significant wave heights fell below 10 cm are spurious due to the depth of the pressure sensor.

Turbulent fluxes were calculated using velocity cospectra from the sonic anemometer and the vertical

array of ADVs. Atmospheric measurements of wind stress were calculated by integrating velocity cospectra for frequencies less than 2 Hz in 30-min blocks (Rieder et al. 1994). A 30-min window should provide a sufficient range of sampling scales to properly represent turbulence in the near-surface atmosphere (Drennan et al. 2003). The sensitivity of vertical flux measurements to variations in sensor orientation prompted a tilt correction using the planar fit method (Wilczak et al. 2001) on daily subranges of the anemometer data as described in Fisher et al. (2015). To avoid artificial enhancement of stress estimates from correlated wave orbital velocities, the integration of ADV burst velocity cospectra was limited to frequencies less than 0.1 Hz, below the wave band. Scully et al. (2015, 2016) analyzed the same data presented here and showed that low-frequency motions, below the wave band, dominate the Reynolds stress tensor.

b. Simulating the surface wave energy budget

A third-generation numerical wave model, Simulating Waves Nearshore (SWAN, version 40.91; Booij et al. 1996), was used to examine the wave energy budget at the tower site. The nonstationary model solves the spectral action density equation on a 5-min computational time step:

$$\frac{\partial N}{\partial t} + \nabla \cdot [(\mathbf{C}_g + \mathbf{U})N] + \frac{\partial c_\sigma N}{\partial \sigma} + \frac{\partial c_\theta N}{\partial \theta} = \frac{1}{\sigma}(S_{\text{wind}} + S_{\text{wcap}} + S_{\text{bot}} + S_{\text{nl3}} + S_{\text{nl4}}), \quad (10)$$

where N is action density (F/σ); $\mathbf{C}_g$ and $\mathbf{U}$ are group velocity and barotropic current velocity, respectively; σ is angular frequency; θ is direction; and S denotes source terms. The first term on the left-hand side is the time rate of change of action density, the second term is the horizontal divergence of wave energy transport, and the next two terms are associated with the divergence of wave energy in wavenumber space due to frequency shifting (term 3) and refraction/diffraction (term 4). The source terms represent the sum of wind energy input S_{wind}, whitecapping dissipation S_{wcap}, bottom-induced frictional dissipation S_{bot}, and nonlinear wave–wave interactions associated with triads S_{nl3} and quadruplets S_{nl4}.

The model was set up as described in Fisher et al. (2015). Wind-wave generation was forced by an optimally interpolated, 10-m, neutral wind field generated from over 60 surface stations in and around Chesapeake Bay. Overland stations were corrected to 10-m neutral conditions using a standard power law (Panofsky and Dutton 1984), and overwater stations were adjusted using the COARE 3.0 algorithm (Fairall et al. 2003). A universal kriging scheme with algorithmically fit exponential variogram was applied to the vector components of the 10-m neutral wind field on a 30-min time step. Wave growth was formulated using the Zijlema et al. (2012) expression for the drag coefficient in combination with the Komen et al. (1984) expression for exponential wave growth. The model accounted for tidal elevation interpolated from nine tide gauges around the Chesapeake Bay, and bottom friction was estimated through the empirical JONSWAP model (Hasselmann et al. 1973). Barotropic currents were not included in the model.

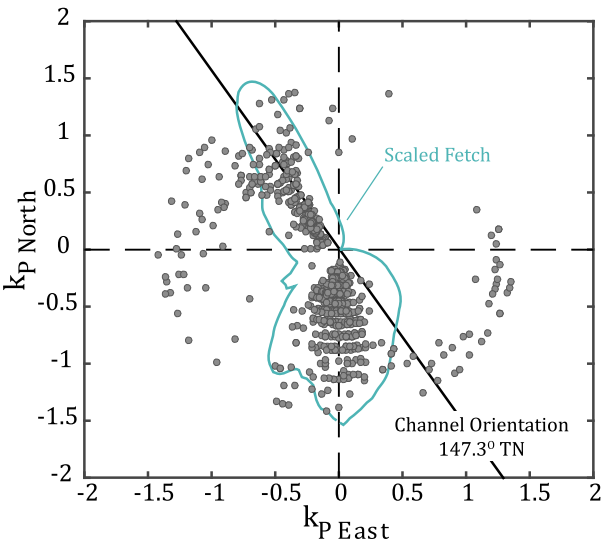

FIG. 4. Tower wave data plotted in wavenumber space where k_{p_east} and k_{p_north} are the wavenumber vector components at the spectral peak. The blue line is a contour of log-transformed fetch scaled to fit. The channel orientation at the tower site is shown as a solid black line.

4. Results and discussion

a. Wind-wave dynamics

An important feature of the surface conditions observed during the deployment was that wind and waves were consistently misaligned during the 10-day nor'easter wind event. During the event, the dominant waves were aligned roughly 17° to the left of the wind [Fig. 3 (bottom)]. Plotting directional wave data in wavenumber space reveals that wave directions measured in the midbay bifurcate along two dominant directions: waves propagating down-estuary generally move south, while waves propagating up-estuary align ~330°T (Fig. 4). Wavenumbers are calculated using the peak period and peak wave direction from directional spectra. The blue line shows log-transformed fetch (scaled to fit) as a function of direction. Fetch was

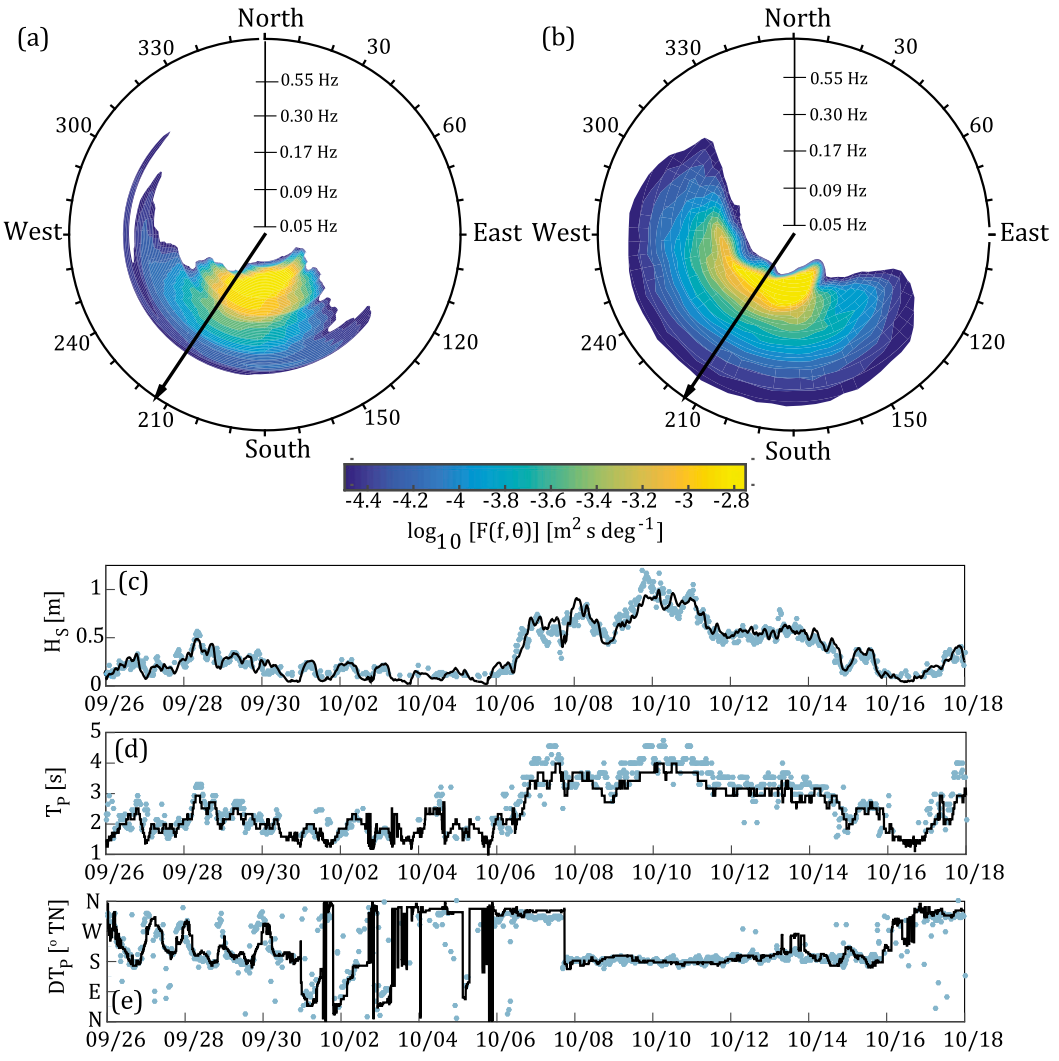

FIG. 5. Model validation. (a) Observed directional wave spectra at tower at 1030 EST 10 Oct 2013 with wind direction shown as a black vector. (b) Modeled spectra for same time period. SWAN captures the peak characteristics of the spectra but slightly overpredicts directional spreading. Observed (blue) and simulated (black) significant (c) wave height, (d) peak period, and (e) peak direction are shown.

calculated as the upwind distance to shore using elevation data used in the SWAN wave model. As waves mature (wave age increases), they concentrate on two principal directions that correspond to the direction of maximum upwind fetch. This behavior is consistent with the slanting fetch observations presented by Donelan et al. (1985) and Ardhuin et al. (2007). Observed waves were predominantly deep-water waves with only a brief period when the wavelength λ was slightly greater than twice the water depth, so depth-induced refraction was not a significant factor in the misalignment between wind and waves. Rather, the misalignment between wind and waves is the result of preferential wave growth along the dominant fetch axes of the embayment.

SWAN model results accurately simulate measured significant wave height, period, and direction, as shown in Fig. 5. The model slightly overpredicts the directional spread of wave energy but accurately captures the mean direction and the change in direction between low and high frequencies seen in the directional wave spectra measured by the uppermost ADV. Analysis of SWAN model output for the tower site shows that the dominant terms in the wave energy budget are wind input, whitecapping dissipation, and the horizontal divergence of wave energy transport. The sum of whitecapping dissipation and the divergence of wave energy transport balance wind input to first order (Fig. 6). This suggests that spatial gradients developed principally through

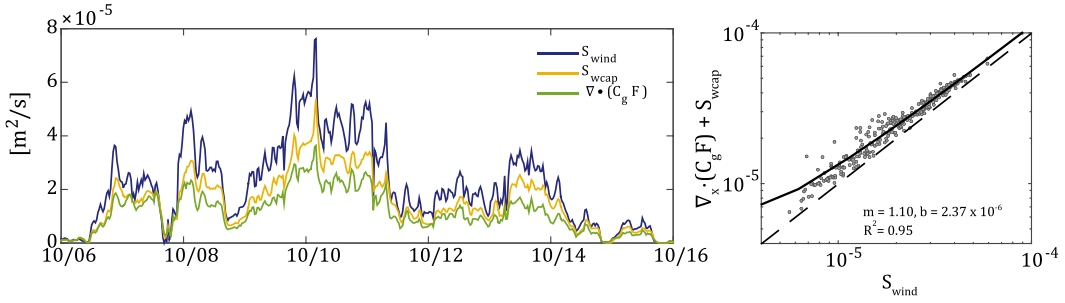

FIG. 6. (left) Time series of simulated wind energy input (blue), whitecapping dissipation (yellow), and horizontal divergence of wave energy transport (green). (right) Simulated wave energy budget at the tower site. Whitecapping dissipation and the horizontal divergence of wave energy transport balance wind input to first order.

directionally variable fetch limitation can result in a significant divergence of wave energy transport. This horizontal divergence of wave energy transport may play an important role in the local air–sea momentum budget associated with a fetch-limited wind sea that is in a state of active growth.

Several studies have shown that swell can affect the direction of wind stress in the atmospheric surface boundary layer (Rieder et al. 1994; Drennan et al. 1999; Potter et al. 2015). However, the upper Chesapeake Bay is characterized as a pure wind-sea environment, such that wave energy in the upper bay is entirely generated by local winds, with any incoming ocean swell dissipating to negligible energy levels by the time it reaches the midbay (Lin et al. 2002). Phillips (1985) hypothesized that a portion of the wind-sea spectrum would be in equilibrium with wind forcing, such that the source terms in Eq. (10) would sum to zero. This "equilibrium range" occurs well above the peak frequency in the wave subrange that supports the majority of the atmospheric wind stress. Following Banner (1990), we define the equilibrium subrange as $f > 2f_p$.

The shear velocity required to maintain equilibrium can be described using the following relation (Thomson et al. 2013):

$$u_{\mathrm{eq}} = \left(\frac{1}{f_{\max} - 2f_p}\right) \int_{2f_p}^{f_{\max}} 8\pi^3 f^4 F(f)\, df, \qquad (11)$$

where f_p is the peak frequency, and $f_{\max}$ is the highest observed/modeled frequency. We calculated this equilibrium shear velocity from observational spectra truncated at 0.6 Hz, averaged over the equilibrium range, and compared the results to shear velocities measured by the sonic anemometer. Bin-averaged results for the 10-day storm event are shown in Fig. 7. For small to moderate stress values, the strong 1:1 correlation of the equilibrium shear velocity and the measured shear velocity indicates that the wave field is in equilibrium with the wind. At large, measured stress values, however, the shear velocity measured by the sonic anemometer is higher than the equilibrium shear velocity calculated from wave spectra. This indicates that the surface wave field is not in equilibrium with the wind and that short gravity waves are in an active state of growth toward equilibrium. The threshold behavior shown in the comparison of the equilibrium shear velocity and the measured shear velocity could be the result of bounded wave growth due to fetch limitation. Because the peak frequency is limited by fetch, the equilibrium shear velocity calculated from Eq. (11) is therefore also limited, resulting in large wind events producing very young seas that never fully saturate.

Additionally, simulated wave spectra were used to calculate the average wave direction as a function of frequency for times when the mean wind direction and wave directions were aligned and misaligned. Figure 8 shows

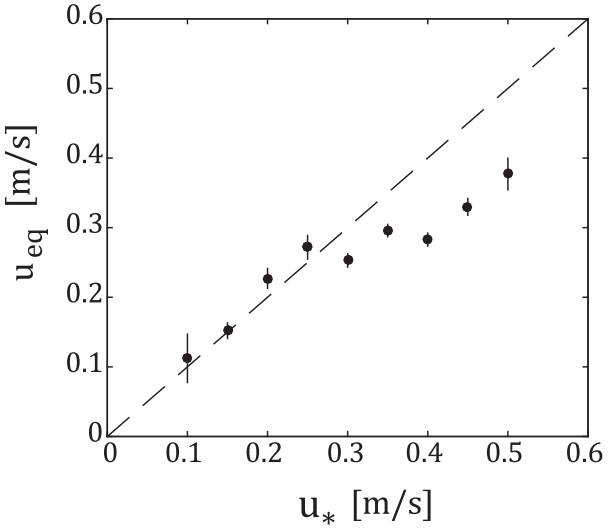

FIG. 7. Bin-averaged comparison of equilibrium shear velocity calculated from observational wave spectra to measured wind shear velocity shown with standard error bars. Equilibrium shear velocity values were calculated as the average of Eq. (11) over the equilibrium subrange of wave spectra ($f > 2f_p$).

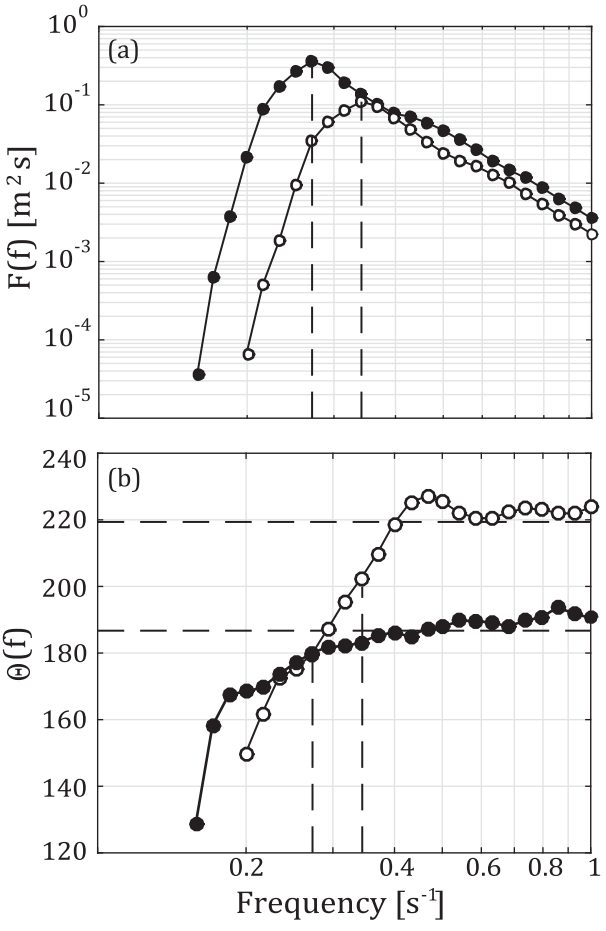

FIG. 8. (a) Modeled wave energy spectra for a period when wind and waves were aligned (black dots) and when they were misaligned (white dots). Peak frequency shown as a dashed line. (b) Average wave direction as a function of frequency for the same periods. Horizontal dashed lines indicate wind direction.

that misalignment between wave direction and wind direction is predominantly a characteristic of wave frequencies at or below the peak, with the quasi-equilibrium range being aligned with wind forcing. Modeled results were used in Fig. 8 instead of observational spectra to present qualitative spectral structure that included frequencies above 0.6 Hz. Observational spectra showed a similar qualitative structure, but the average direction within the equilibrium subrange was significantly noisier than that calculated from simulated spectra.

b. *Stress dynamics across the air–sea interface*

As discussed in Scully et al. (2016), the direction of the momentum flux vector changed across the air–sea interface. Direct measurements from the ultrasonic anemometer show that the stress in air is aligned with mean wind direction, with an average departure angle of 2.2° ± 1.2° to the left of the wind. In contrast, the stress at the uppermost ADV ($z = -1.7$ m depth) is more aligned with wave forcing than wind forcing with a mean departure angle of 16.07° ± 1.8° to the left of the wind. These results are consistent among the top four ADVs, suggesting that the momentum flux vector in the surface layer of the estuary is misaligned with local wind forcing and may be controlled by the surface wave field.

Figure 9a shows the distributions of departure angles, clockwise relative to wind forcing, of the momentum flux vector measured in air θ_{air}, the momentum flux vector measured in water $\theta_{z=-1.7m}$, and peak wave direction θ_{waves}. Figure 9b shows a mean vector stress profile averaged over the same period, which shows that the turning of the momentum flux vector across the air–sea interface is counterclockwise. Conversely, a clear clockwise rotation is present in the vertical stress profile of the surface layer of the estuary. The width of the midbay is the same order as the internal Rossby radius, so this clockwise rotation is likely indicative of Ekman steering within the well-mixed surface layer.

During the wind event, persistent near-bottom stratification was present for depths greater than ~10 m and limited the vertical extent of the bottom boundary layer (Scully et al. 2015). The stress direction within this bottom boundary layer, measured by the lowest tower ADV ($z = -11.5$ m) and a collocated bottom lander, was tidally dominated and is not shown in Fig. 9b.

The vector difference between stress measured above ($z = 2.8$ m) and below ($z = -1.7$ m) the air–sea interface changes with the misalignment between surface gravity waves and wind. As shown in Fig. 10, the across-wave (defined using the peak wave direction) component of the wind stress is increasingly larger than the across-wave component of the marine stress as the angle between waves and wind increases up to a maximum at about 40° misalignment. In contrast, the differences between along-wave components of stress are much less than that of across-wave components and do not exhibit a significant change with regards to the angle between wind and waves. The observed differences in stress direction and magnitude measured across the air–sea interface indicate that the local momentum budget between the atmosphere and the mean flow at the tower site is not closed and that the surface wave field likely plays an important role in the translation of stress across the air–sea interface.

c. *Surface waves and the local air–sea momentum budget*

Using interaction stress theory, measured wind stress and modeled terms in the wave energy budget were used to approximate the fraction of the momentum flux stored in (or released by) the surface wave field following Ardhuin et al. (2004):

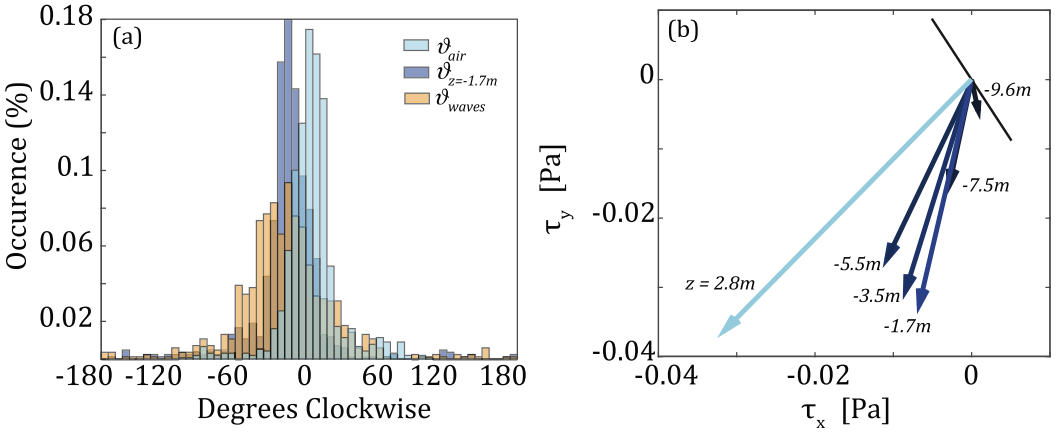

FIG. 9. (a) Distributions of the departure angle of the momentum flux vector measured in air (ϑ_{air}; light blue) and at $z = -1.7$ m ($\vartheta_{z=-1.7\text{m}}$; dark blue) from mean local wind direction measured clockwise. The distribution of the angle between wind and waves at the tower site is also shown (ϑ_{waves}; orange). (b) Average momentum flux vectors showing the departure of the marine stress profile from the atmospheric surface stress in geographic coordinates. Black line denotes principal tidal axis (150° T).

$$\tau_\alpha^{\text{air}} - \tau_\alpha^{\text{int}} = \int \left[(S_{\text{wind}} + S_{\text{wcap}} + S_{\text{nl}}) \frac{k_\alpha}{kC} - \frac{C_{k,\beta}}{C} \left(\frac{\partial F}{\partial k_\beta} \right) \right] + \frac{\partial}{\partial x_\beta} \left[F \left(\frac{1}{2} - \frac{C_g k_\alpha k_\beta}{Ck^2} \right) \right] \mathbf{dk}, \tag{12}$$

which is derived by dividing Eq. (10) by the phase speed and integrating over the wavenumber vector k. Note that the above equation is equivalent to Eq. (8), where the last term on the right-hand side is the divergence of a depth-averaged, wave-induced stress in the wavy surface layer due to the dynamic pressure associated with a fluctuating instantaneous free surface and the wave component of the Reynolds stress. Because our model results indicate that refraction and frequency shifting effects due to depth variations are very small relative to other terms in the wave energy budget, we neglect the second term in the first pair of brackets in Eq. (12).

Before proceeding with an analysis of the interaction stress, we note that our modeled interaction stress was significantly higher than the atmospheric stress at the onset of the 10-day nor'easter event, which is likely due to an overprediction of wave energy during that period. A sheltering effect is expected for winds blowing out of the south-southwest due to a 30-m topographic feature, Calvert Cliffs. The cliffs likely created an internal boundary layer adjustment that reduced surface atmospheric

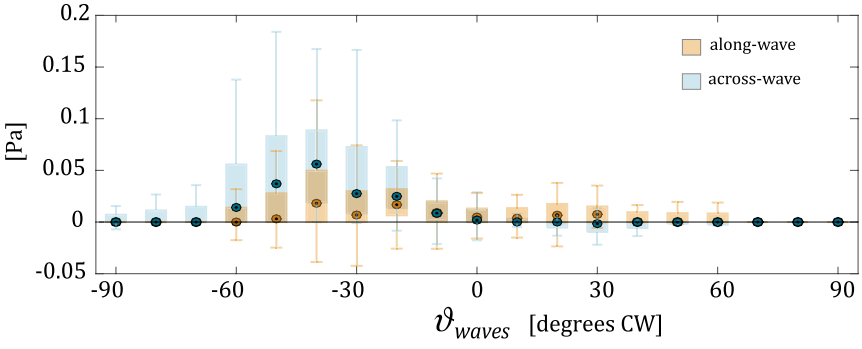

FIG. 10. Vector difference between stress measured in air ($z = 2.8$ m) and stress measured in water ($z = -1.7$ m) vs the observed angle between the wind and peak wave direction ϑ_{waves} As the misalignment between wind and waves increases [more negative clockwise (CW)], the difference between the measured cross-wave stress above and below the air–sea interface also increases.

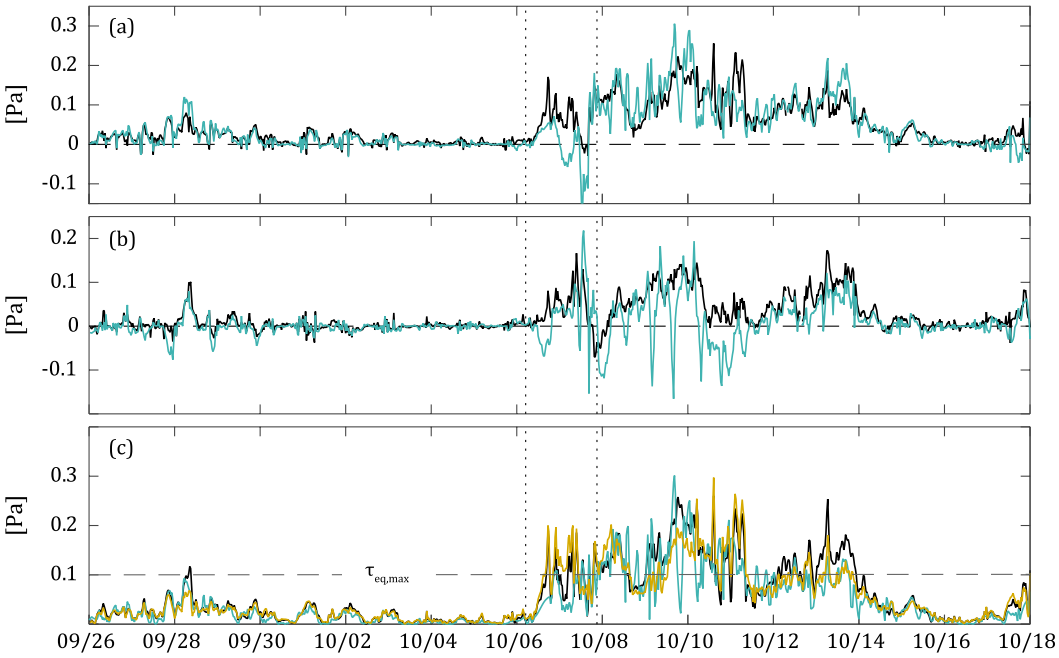

FIG. 11. Time series comparison of (a) along-wave components of the τ^{air} (black) and $\tau^{z=-1.7m} + (\tau^{air} - \tau^{int})$ (blue), (b) across-wave components of the τ^{air} (black) and $\tau^{z=-1.7m} + (\tau^{air} - \tau^{int})$ (blue), and (c) magnitudes of τ^{air} (black), τ^{int} (yellow), and $\tau^{z=-1.7m}$ (blue). Vertical dotted lines indicate a period when SWAN overpredicted wave energy. Horizontal dashed line in (c) represents maximum observed stress at which the observed wave field was in equilibrium with local wind forcing.

stress 1–2 km away from the shoreline (Markfort et al. 2010). For this reason, we omit the period between 1000 eastern standard time (EST) 6 October to 0000 EST 8 October from further analysis.

Using a wave-aligned coordinate system in which x is the direction of dominant wave propagation and y is parallel to wave crests, we examine the air–sea momentum budget across the air–sea interface by comparing the atmospheric stress τ^{air}, interaction stress τ^{int}, and the stress measured at the uppermost ADV at $z = -1.7$ m $\tau^{z=-1.7m}$. To make comparisons more direct, we scale τ^{air} and τ^{int} using linear surface layer stress scaling for a wall-bounded shear flow based on the depth of the mixed surface layer (~10 m):

$$\tau^z = \tau^0 \left(1 - \frac{|z|}{h}\right), \tag{13}$$

where τ^0 is the stress at the mean free surface, and h is the height of the boundary layer. This scaling of stress has been demonstrated to hold for the outer log layer and assumes a balance between shear production and dissipation (Tennekes and Lumley 1972). Turbulent kinetic energetics beneath breaking waves differ from those in a neutral log layer and are often described as a balance between divergent TKE transport and dissipation (Terray et al. 1996). However, the large-eddy simulation (LES) results of Sullivan et al. (2007) show a similar linear distribution of stress beneath energetic wave breaking, and, as Scully et al. (2016) also showed, a surface layer scaling of stress accurately represents our observations of stress within the oceanic surface boundary layer during periods of active wave forcing.

The time series of the along-wave components and cross-wave components of the local air–sea momentum budget are shown in Fig. 11, along with the magnitude of the total wind stress, the marine stress at $z = -1.7$ m, and the interaction stress. In Figs. 11a and 11b, we have included the effects of surface gravity waves through the addition of the value of $\tau^{air} - \tau^{int}$ estimated from Eq. (12) to the along-wave x and cross-wave components y of the stress at $z = -1.7$ m.

The total interaction stress magnitude was often less than the atmospheric stress but consistent with the total stress measured at the uppermost ADV, suggesting that a significant portion of the atmospheric stress was not translated to a momentum flux within the surface layer of the estuary when dominant waves were misaligned with moderate to strong local wind forcing. The dashed horizontal line in Fig. 11c represents the maximum stress at which the wave field was in equilibrium with local wind forcing (Fig. 7): $\tau_{eq,max} = 0.1$ Pa.

Effectively, the threshold behavior shown in Fig. 11c represents that point at which the total wind stress exceeded the stress that could be translated through the wave field to the mean flow, which is determined by fetch limitation at the tower site.

At the end of the nor'easter, between 12 and 14 October when the wind and waves were significantly misaligned, the stress measured at $z = -1.7$ m was at times only half the stress measured at $z = 2.8$ m. The addition of the wave storage/release term $\tau^{air} - \tau^{int}$ to the vector components of the measured marine stress improved the agreement between the time series of stress across the air–sea interface and accounted for the observed differences in the momentum flux (Figs. 11a,b). These results indicate that momentum storage (or release) associated with the growth (decay) of a wind sea accounted for the observed stress differences.

In Fig. 12, we present a vector momentum budget across the air–sea interface that accounts for the growth of wind waves through interaction stress theory. We limit the analysis to periods when the atmospheric shear velocity exceeded 0.103 m s^{-1} and $\theta_{waves} > 20°$ to isolate periods when a significant stress divergence occurred across the air–sea interface. In the along-wave direction, a balance exists between the interaction stress and the stress measured at $z = -1.7$ m, assuming surface layer scaling (Fig. 12a). In the cross-wave direction, the sum of the stress measured by the ADV and the storage of momentum in the surface wave field $|\tau^{air} - \tau^{int}|$ balance the cross-wave component of the atmospheric stress vector (Fig. 14b). This indicates that the storage of momentum in the surface wave field occurred orthogonal to the direction of dominant wave propagation and that the observed difference in stress measured across the air–sea interface is directly attributable to the growth of a misaligned wind sea.

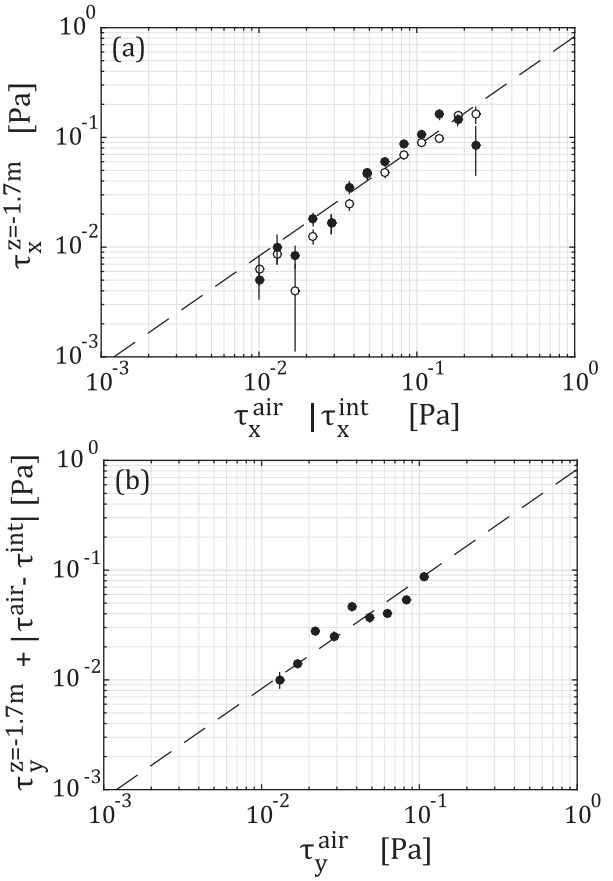

FIG. 12. Bin-averaged comparison of (a) along-wave components of the interaction stress (black) and the atmospheric stress (white) to the along-wave component of the stress vector measured at $z = -1.7$ m shown with standard error bars. (b) A comparison between the cross-wave atmospheric stress and the sum of the measured cross-wave stress at $z = -1.7$ m and the momentum stored in the surface wave field ($\tau^{air} - \tau^{int}$). The dashed line in both subplots represents surface layer scaling.

A strong correlation exists between this wave storage/release term and mean wind direction. Figure 13 shows the difference between τ^{air} and τ^{int} plotted as a function of wind direction. When winds blow across dominant fetch axes at moderate to high wind speeds, the generation of short gravity waves in the direction of wind forcing serves as a sink of momentum and can store a significant fraction of the air–sea momentum flux ($\tau^{air} > \tau^{int}$). Conversely, when winds blow along dominant fetch axes (~180°T or 330°T), the surface wave field enhances the flux of momentum into the mean flow by releasing momentum through the dissipation of remote wave energy ($\tau^{air} < \tau^{int}$). For periods when there was little momentum storage/release in the surface wave field ($|\tau^{air} - \tau^{int}| <$ 0.03 Pa), the effects of wind direction on wave storage versus wave release become less clear because the wave field at the tower site was likely near fully saturated (Fig. 7).

In steady-state wind seas, breaking wave energy that exceeds wind input would not make sense. A closer look at the ''wave release'' period reveals that it corresponds to a brief relaxation in wind forcing and a period when wave energy at the tower site was decreasing. This suggests that estimated release values may be the result of a decaying wind sea. While these results are specific to the middle reaches of Chesapeake Bay, similar dynamics stemming from anisotropic fetch limitation may be common in coastal environments.

The dynamics of momentum storage in the surface wave field are best understood by looking at the time series of terms in Eq. (12) (Fig. 14). Throughout the 10-day event, the dominant term on the right-hand side

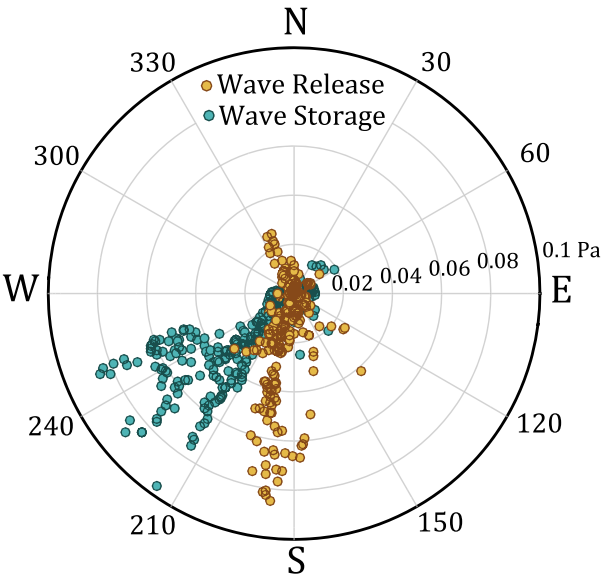

FIG. 13. The $\tau^{air} - \tau^{int}$ plotted as a function of wind direction. When winds blow across the dominant fetch axes of the estuary the surface wave field stores momentum; when winds blow along the dominant fetch axes waves enhance the air–sea momentum flux through the dissipation of remote wave energy. Note that light winds ($\tau < 0.03$ Pa) do not exhibit the same directional tendencies.

of Eq. (12) is the horizontal divergence of the surface Reynolds stress in the wavy surface layer

$$\frac{\partial}{\partial x_\beta}\left[F\left(\frac{1}{2} - \frac{C_g k_\alpha k_\beta}{Ck^2}\right)\right]$$

due to gravity waves. In a depth-integrated form, the horizontal divergence of the Reynolds stress associated with a wavy free surface is the result of anisotropic wave momentum being advected by wave velocities (Ardhuin et al. 2004). This divergence is therefore directly associated with the growth and decay of wave energy within a surface wave field. For a wave field in equilibrium with wind forcing, this suggests that local wave energy growth balances a divergence in the transport of nonlocal energy. For non-steady-state conditions, this term represents a significant portion of local wave energy change that is not due to an imbalance in local source terms (Fig. 6). This, in combination with the results shown in Figs. 11–13, suggests that differences in stress between the sonic anemometer and uppermost ADV are directly attributable to the momentum fluxes associated with the growth of a fetch-limited wind sea and that the degree of fetch limitation depends strongly on both wind speed and wind direction.

d. *Wave-driven turbulence and the direction of the marine stress vector*

While the previous section clearly showed that modulation of air–sea momentum transfer by the directional growth or decay of the wave field due to fetch limitation can account for differences between applied wind forcing and the resultant marine stress vector, we have not yet addressed the mechanism through which wind stress at the surface is transferred into the water column. Conceptually, there are two modes of momentum exchange driven by breaking surface waves: 1) impulses of momentum associated with whitecapping waves that aggregate to produce a mean stress in the direction of wave breaking (Sullivan et al. 2004) and 2) momentum transfer associated with the vertical transport of near-surface momentum by intensified downwelling jets

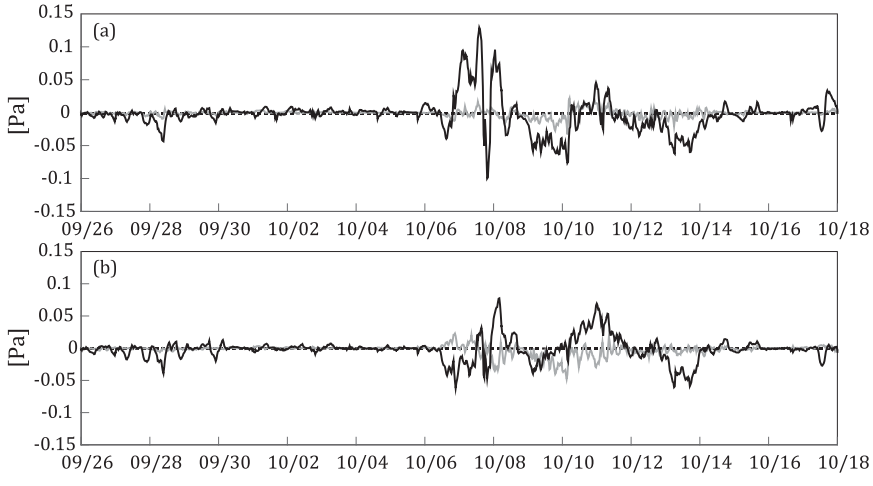

FIG. 14. (a) East–west component and (b) north–south component time series of source term (gray) and stress divergence (black) terms used in calculation of $\tau^{air} - \tau^{int}$. Note that stress divergence is dominant throughout the deployment.

associated with Langmuir turbulence (McWilliams et al. 1997; Kukulka et al. 2010; Kukulka et al. 2012; Sullivan et al. 2012). It has been shown that Langmuir turbulence cells align predominantly with vertical shear in the Lagrangian velocity, defined as the sum of the Eulerian velocity and the Stokes drift velocity associated with wave orbital velocities. This shear strains the vorticity field generated beneath breaking waves (Leibovich 1983; McWilliams et al. 1997; Van Roekel et al. 2012; Sullivan et al. 2012; Rabe et al. 2015). Therefore, the relative roles of breaking impulses and mean total shear in determining the stress direction in the surface layer of the estuary can be qualitatively addressed using the observed directions of wave breaking, Lagrangian shear, and the Reynolds stress in the surface layer of the estuary.

We evaluated the mean nonlinearity of dominant wind waves observed during the deployment using the significant steepness parameter suggested by Banner et al. (2000). Throughout the 10-day wind event, the dominant wind-wave steepness exceeded (often by a factor of 2) the breaking threshold of 0.055 proposed by Banner et al. (2000). The downward sweep of momentum resulting from breaking waves would have occurred primarily in the direction of dominant wave propagation, which is consistent with the agreement between the mean direction of the marine stress vector and the mean direction of wave propagation. However, the observed stress direction at $z = -1.7$ m was at times more than 20° different from the direction of dominant wave propagation, suggesting that dominant wave breaking alone cannot explain the temporal variability in stress direction.

We investigate the importance of Lagrangian shear in momentum exchange within the surface layer of the estuary by estimating the Stokes drift profile from directional spectra following Kenyon (1969):

$$U_{\text{stokes}}(z) = \int_0^{2\pi}\int_0^{\sigma_{\max}} F(\sigma,\theta)\sigma k \frac{\cosh[2k(h+z)]}{\sinh^2[k(h+z)]}\cos(\theta_{\text{waves}})\,\partial\sigma\,\partial\theta, \tag{14}$$

where $F(\sigma, \theta)$ is the directional wave spectrum, σ is the frequency, and θ_{waves} is the angle between wind and waves. We can estimate the direction of Lagrangian shear in the surface layer of the estuary by taking a depth average of the sum of crosswind v Eulerian and Stokes drift shear divided by the sum of the along-wind u Eulerian and Stokes drift shear (Van Roekel et al. 2012):

$$\theta_{S_L} = \text{atan}\left(\frac{\left\langle \frac{\partial V}{\partial z} + \frac{\partial V_{\text{stokes}}}{\partial z}\right\rangle_z}{\left\langle \frac{\partial U}{\partial z} + \frac{\partial U_{\text{stokes}}}{\partial z}\right\rangle_z}\right). \tag{15}$$

Averaging over the upper 5 m of the water column, indicates that the direction of Lagrangian shear in the estuarine surface layer agrees with the inferred angle of Langmuir cells observed during the deployment (Scully et al. 2015). Numerical simulations have also shown that the orientation of Langmuir turbulence is aligned with the direction of Lagrangian shear in the surface layer (Sullivan et al. 2012; Van Roekel et al. 2012).

A comparison of measured stress direction at $z = -1.7$ m and observed wind, wave, and shear conditions is shown in Fig. 15. The time series of stress direction, wave direction, wind direction, and shear direction show that while the marine stress mean direction agrees well with the mean direction of dominant wave propagation, the temporal variability of the marine stress direction is much better predicted by the direction of the Lagrangian shear in the surface layer of the estuary. Based on this observation, we hypothesize that breaking waves were the primary pathway through which momentum was transferred between the air and the oceanic surface layer but that Langmuir turbulence likely played an important role in momentum transfer deeper within the oceanic surface boundary layer.

While numerous studies have shown that Stokes production is often a dominant term in the TKE budget during times when Langmuir turbulence is present (McWilliams et al. 2012; Rabe et al. 2015), an analysis of the TKE budget on this dataset indicates that the pressure work was the dominant transport term and balanced dissipation to first order in the surface layer of the estuary (Scully et al. 2016). More detailed analysis of turbulent energetics observed during this experiment can be found in Scully et al. (2016; A. W. Fisher et al. 2017, unpublished manuscript). Despite the generation of TKE due to Stokes drift production being small compared to the flux of energy imparted by breaking waves, the stretching and tilting of vertical vorticity by the Stokes drift velocity is an important physical process that has significant implications for momentum exchange beneath breaking waves (Kukulka et al. 2012). Nonlocal transport by coherent large-scale eddies may carry momentum away from a surface source, along the gradient of vertical Lagrangian shear, more efficiently than momentum transport due to wave breaking that

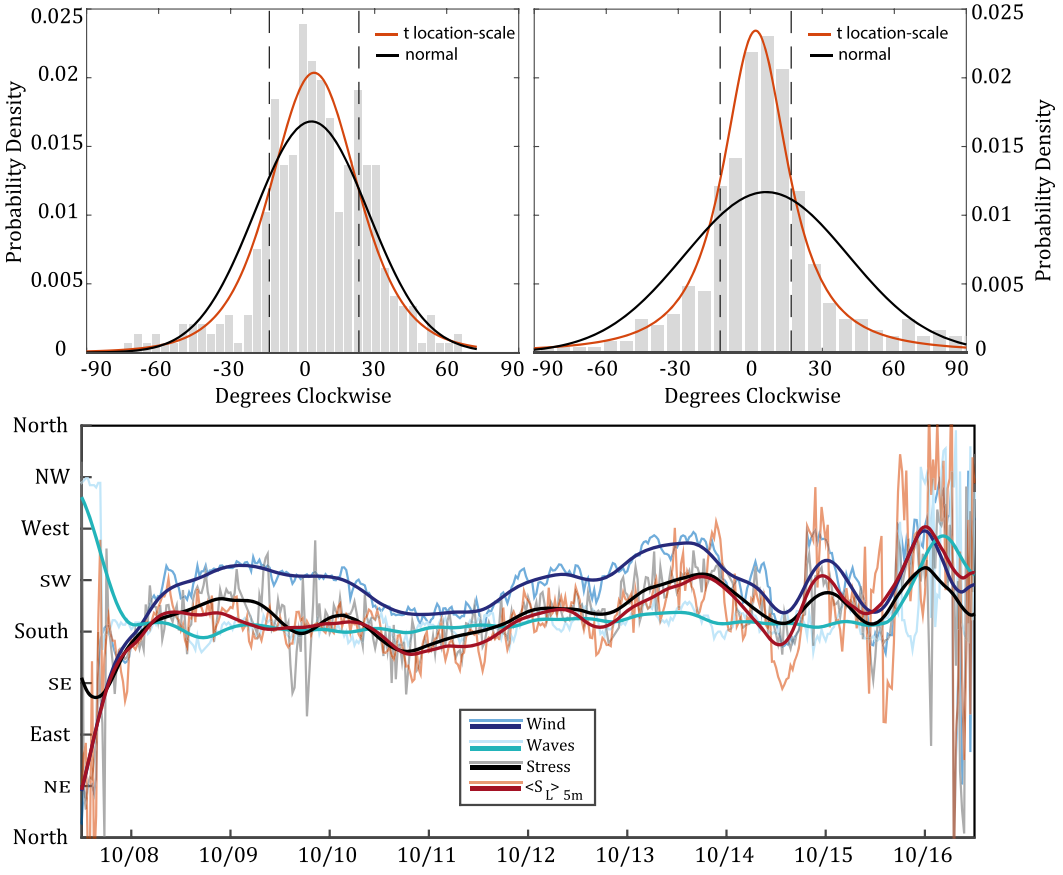

FIG. 15. (top left) Distribution of angle between stress measured at $z = -1.7$ m and peak wave direction shown with normal (black) and t location-scale (red) fits and 1σ confidence intervals. (top right) Distribution of angle between stress measured at $z = -1.7$ m and the Lagrangian shear direction in the surface layer of the estuary shown with normal (black) and t location-scale (red) fits and 1σ confidence intervals. (bottom) Time series of low-pass filtered directions of wind (dark blue), wave (light blue), stress at $z = -1.7$ m (black), and depth-averaged Lagrangian shear (red) for a 10-day nor'easter in October 2013. The direction of the momentum flux vector at the uppermost ADV is closely correlated to the direction of Lagrangian shear in the surface layer of the estuary.

mimics turbulent transport under free shear conditions (e.g., Craig and Banner 1994).

5. Conclusions

Anisotropic fetch limitation in the middle reaches of Chesapeake Bay results in an environment where wind and waves are commonly and persistently misaligned. Although pure wind seas characterize the midbay, directional wave spectra show that dominant waves develop along the dominant fetch axes of the estuary and may be significantly misaligned with the wind. Direct measurements of the momentum flux collected above and below the water surface indicate that the surface wave field plays an important role in the local air–sea momentum budget beyond simply the enhancement of surface fluxes associated with increased drag at the water surface and/or the injection of TKE by breaking waves.

The stress vector in the surface layer of the estuary was aligned more with wave forcing than wind forcing and was highly correlated to the direction of Lagrangian shear in the upper 5 m of the water column. An apparent stress divergence occurs between the ultrasonic anemometer ($z \sim 2.8$ m) and the uppermost ADV ($z \sim -1.7$ m), such that the direction and magnitude of the momentum flux vector changes across the air–sea interface. Using the interaction stress theory described by Hasselmann (1971) and Ardhuin et al. (2004), we address the role of the surface wave field in the local air–sea momentum budget by partitioning the momentum flux between surface gravity waves and the mean flow. The interaction stress magnitude compares well to the magnitude of the momentum flux measured at the

uppermost ADV, assuming a linear surface layer scaling of stress. Additionally, results indicate that the surface wave field can store a significant fraction of the momentum flux, up to 30%–40%, at times when the wind blows across dominant fetch axes.

Fetch limitation results in bounded wave growth, which for large wind events can result in very young seas that are not in equilibrium with wind forcing. The generation of short gravity waves dominates the drag felt by the wind field and may serve as a momentum sink in the local momentum budget of the oceanic surface boundary layer. This is especially true when dominant, longer waves are misaligned with wind forcing. An analysis of the wave momentum evolution equation using a third-generation wave model and direct observations of wind stress indicate that the stress fraction stored in/released by the surface wave field is dominated by the horizontal stress divergence associated with a wavy instantaneous free surface.

While the interaction stress properly accounts for differences in stress that occur across the air–sea interface, the direction of the stress vector in the surface layer of the estuary requires further explanation. The authors hypothesize that the vorticity field generated by breaking waves is strained in the direction of the Lagrangian shear in a manner similar to Langmuir turbulence.

This Lagrangian shear does not significantly enhance the generation of near-surface turbulence but rather modifies vertical transport regimes that act to control the direction of the stress tensor in the surface layer of the estuary.

While the details of this manuscript are specific to the middle reaches of Chesapeake Bay, the trends presented suggest that further research is needed in fetch-limited, coastal environments where the tendency for misaligned wind and wave fields may be common. These results indicate that the surface wave field can significantly affect the translation of wind stress across the air–sea interface and may play an important role in coastal momentum budgets.

Acknowledgments. This manuscript benefited greatly from the comments and suggestions of Dr. Bill Boicourt and two anonymous reviewers. This work was supported by National Science Foundation Grants OCE-1061609 and OCE-1339032.

REFERENCES

Agrawal, Y. C., E. A. Terray, M. A. Donelan, P. A. Hwang, A. J. Williams III, W. M. Drennan, K. K. Kahma, and S. A. Kitaigorodskii, 1992: Enhanced dissipation of kinetic energy beneath surface waves. *Nature*, **359**, 219–220, doi:10.1038/359219a0.

Ardhuin, F., B. Chapron, and T. Elfouhaily, 2004: Waves and the air–sea momentum budget: Implications for ocean circulation modeling. *J. Phys. Oceanogr.*, **34**, 1741–1755, doi:10.1175/1520-0485(2004)034<1741:WATAMB>2.0.CO;2.

——, T. H. C. Herbers, K. P. Watts, G. P. van Vledder, R. Jensen, and H. C. Graber, 2007: Swell and slanting-fetch effects on wind wave growth. *J. Phys. Oceanogr.*, **37**, 908–931, doi:10.1175/JPO3039.1.

Banner, M. L., 1990: Equilibrium spectra of wind waves. *J. Phys. Oceanogr.*, **20**, 966–984, doi:10.1175/1520-0485(1990)020<0966:ESOWW>2.0.CO;2.

——, A. V. Babanin, and I. R. Young, 2000: Breaking probability for dominant waves on the sea surface. *J. Phys. Oceanogr.*, **30**, 3145–3160, doi:10.1175/1520-0485(2000)030<3145:BPFDWO>2.0.CO;2.

Booij, N., L. H. Holthuijsen, and R. C. Ris, 1996: The "SWAN" wave model for shallow water. *Proc. 25th Conf. on Coastal Engineering*, Orlando, FL, ASCE, 668–676. [Available online at https://icce-ojs-tamu.tdl.org/icce/index.php/icce/article/view/5257.]

Charnock, H., 1955: Wind stress on a water surface. *Quart. J. Roy. Meteor. Soc.*, **81**, 639–640, doi:10.1002/qj.49708135027.

Chen, S.-N., and L. P. Sanford, 2009: Axial wind effects on stratification and longitudinal salt transport in an idealized, partially mixed estuary. *J. Phys. Oceanogr.*, **39**, 1905–1920, doi:10.1175/2009JPO4016.1.

——, ——, and D. K. Ralston, 2009: Lateral circulation and sediment transport driven by axial winds in an idealized, partially mixed estuary. *J. Geophys. Res.*, **114**, C12006, doi:10.1029/2008JC005014.

Craig, P. D., and M. L. Banner, 1994: Modeling wave-enhanced turbulence in the ocean surface layer. *J. Phys. Oceanogr.*, **24**, 2546–2559, doi:10.1175/1520-0485(1994)024<2546:MWETIT>2.0.CO;2.

Craik, A. D., 1977: The generation of Langmuir circulations by an instability mechanism. *J. Fluid Mech.*, **81**, 209–223, doi:10.1017/S0022112077001980.

——, and S. Leibovich, 1976: A rational model for Langmuir circulations. *J. Fluid Mech.*, **73**, 401–426, doi:10.1017/S0022112076001420.

D'Asaro, E. A., 2001: Turbulent vertical kinetic energy in the ocean mixed layer. *J. Phys. Oceanogr.*, **31**, 3530–3537, doi:10.1175/1520-0485(2002)031<3530:TVKEIT>2.0.CO;2.

Donelan, M. A., 1982: The dependence of the aerodynamic drag coefficient on wave parameters. *Proc. First Int. Conf. on the Meteorology and Air–Sea Interaction of the Coastal Zone*, The Hague, Netherlands, Amer. Meteor. Soc., 381–387.

——, J. Hamilton, and W. H. Hui, 1985: Directional spectra of wind-generated waves. *Philos. Trans. Roy. Soc. London*, **A315**, 509–562, doi:10.1098/rsta.1985.0054.

Drennan, W. M., K. K. Kahma, E. A. Terray, M. A. Donelan, and S. A. Kitaigorodskii, 1992: Observations of the enhancement of kinetic energy dissipation beneath breaking wind waves. *Breaking Waves*, M. L. Banner and R. H. J. Grimshaw, Eds., Springer, 95–101.

——, M. A. Donelan, E. A. Terray, and K. B. Katsaros, 1996: Oceanic turbulence dissipation measurements in SWADE. *J. Phys. Oceanogr.*, **26**, 808–815, doi:10.1175/1520-0485(1996)026<0808:OTDMIS>2.0.CO;2.

——, K. K. Kahma, and M. A. Donelan, 1999: On momentum flux and velocity spectra over waves. *Bound.-Layer Meteor.*, **92**, 489–515, doi:10.1023/A:1002054820455.

——, H. C. Graber, D. Hauser, and C. Quentin, 2003: On the wave age dependence of wind stress over pure wind seas. *J. Geophys. Res.*, **108**, 8062, doi:10.1029/2000JC000715.

Edson, J. B., and Coauthors, 2013: On the exchange of momentum over the open ocean. *J. Phys. Oceanogr.*, **43**, 1589–1610, doi:10.1175/JPO-D-12-0173.1.

Fairall, C. W., E. F. Bradley, J. E. Hare, A. A. Grachev, and J. B. Edson, 2003: Bulk parameterization of air–sea fluxes: Updates and verification for the COARE algorithm. *J. Climate*, **16**, 571–591, doi:10.1175/1520-0442(2003)016<0571:BPOASF>2.0.CO;2.

Fisher, A. W., L. P. Sanford, and S. E. Suttles, 2015: Wind stress dynamics in Chesapeake Bay: Spatiotemporal variability and wave dependence in a fetch-limited environment. *J. Phys. Oceanogr.*, **45**, 2679–2696, doi:10.1175/JPO-D-15-0004.1.

Geernaert, G. L., K. B. Katsaros, and K. Richter, 1986: Variations of the drag coefficient and its dependence on sea state. *J. Geophys. Res.*, **91**, 7667–7679, doi:10.1029/JC091iC06p07667.

Gemmrich, J. R., 2010: Strong turbulence in the wave crest region. *J. Phys. Oceanogr.*, **40**, 583–595, doi:10.1175/2009JPO4179.1.

——, and D. Farmer, 1999: Observations of the scale and occurrence of breaking surface waves. *J. Phys. Oceanogr.*, **29**, 2595–2606, doi:10.1175/1520-0485(1999)029<2595:OOTSAO>2.0.CO;2.

——, M. L. Banner, and C. Garrett, 2008: Spectrally resolved energy dissipation rate and momentum flux of breaking waves. *J. Phys. Oceanogr.*, **38**, 1296–1312, doi:10.1175/2007JPO3762.1.

Gerbi, G. P., J. H. Trowbridge, J. B. Edson, A. J. Pleuddemann, E. A. Terray, and J. J. Fredericks, 2008: Measurements of momentum and heat transfer across the air–sea interface. *J. Phys. Oceanogr.*, **38**, 1054–1072, doi:10.1175/2007JPO3739.1.

Geyer, W. R., 1997: Influence of wind on dynamics and flushing of shallow estuaries. *Estuarine Coastal Shelf Sci.*, **44**, 713–722, doi:10.1006/ecss.1996.0140.

Harcourt, R. R., and E. A. D'Asaro, 2008: Large-eddy simulation of Langmuir turbulence in pure wind seas. *J. Phys. Oceanogr.*, **38**, 1542–1562, doi:10.1175/2007JPO3842.1.

Hasselmann, K., 1971: On the mass and momentum transfer between short gravity waves and larger-scale motions. *J. Fluid Mech.*, **50**, 189–205, doi:10.1017/S0022112071002520.

——, and Coauthors, 1973: Measurements of wind-wave growth and swell decay during the Joint North Sea Wave Project (JONSWAP). Ergänzungsheft zur Deutschen Hydrographischen Zeitschrift Reihe A(8) 12, 95 pp.

Janssen, P. A. E. M., 1989: Wave-induced stress and the drag of air flow over sea waves. *J. Phys. Oceanogr.*, **19**, 745–754, doi:10.1175/1520-0485(1989)019<0745:WISATD>2.0.CO;2.

Johnson, D., 2002: DIWASP: Directional Wave Spectra toolbox version 1.1 for MATLAB: User manual. Centre for Water Research, University of Western Australia Research Rep. WP 1601 DJ (V1.1), 21 pp.

Johnson, H. K., and H. J. Vested, 1992: Effects of water waves on wind shear stress for current modeling. *J. Atmos. Oceanic Technol.*, **9**, 850–861, doi:10.1175/1520-0426(1992)009<0850:EOWWOW>2.0.CO;2.

——, J. Højstrup, H. J. Vested, and S. E. Larsen, 1998: On the dependence of sea surface roughness on wind waves. *J. Phys. Oceanogr.*, **28**, 1702–1716, doi:10.1175/1520-0485(1998)028<1702:OTDOSS>2.0.CO;2.

Jones, N. L., and S. G. Monismith, 2007: Measuring short-period wind waves in a tidally forced environment with a subsurface pressure gauge. *Limnol. Oceanogr. Methods*, **5**, 317–327, doi:10.4319/lom.2007.5.317.

Kenyon, K. E., 1969: Stokes drift for random gravity waves. *J. Geophys. Res.*, **74**, 6991–6994, doi:10.1029/JC074i028p06991.

Kitaigorodskii, S. A., 1973: *The Physics of Air–Sea Interaction*. Cambridge University Press, 273 pp.

——, M. A. Donelan, J. L. Lumley, and E. A. Terray, 1983: Wave–turbulence interactions in the upper ocean. Part II: Statistical characteristics of wave and turbulent components of the random velocity field in the marine surface layer. *J. Phys. Oceanogr.*, **13**, 1988–1999, doi:10.1175/1520-0485(1983)013<1988:WTIITU>2.0.CO;2.

Komen, G. J., S. Hasselmann, and K. Hasselmann, 1984: On the existence of a fully developed wind-sea spectrum. *J. Phys. Oceanogr.*, **14**, 1271–1285, doi:10.1175/1520-0485(1984)014<1271:OTEOAF>2.0.CO;2.

——, P. A. E. M. Janssen, V. Makin, and W. Oost, 1998: On the sea state dependence of the Charnock parameter. *Global Atmos. Ocean Syst.*, **5**, 367–388.

Kukulka, T., A. J. Plueddemann, J. H. Trowbridge, and P. P. Sullivan, 2010: Mixed layer deepening by the combination of Langmuir and shear instabilities: A case study. *J. Phys. Oceanogr.*, **40**, 2381–2400, doi:10.1175/2010JPO4403.1.

——, ——, and P. P. Sullivan, 2012: Nonlocal transport due to Langmuir circulation in a coastal ocean. *J. Geophys. Res.*, **117**, C12007, doi:10.1029/2012JC008340.

Leibovich, S., 1977: Convective instability of stably stratified water in the ocean. *J. Fluid Mech.*, **82**, 561–581, doi:10.1017/S0022112077000846.

——, 1983: The form and dynamics of Langmuir circulations. *Annu. Rev. Fluid Mech.*, **15**, 391–427, doi:10.1146/annurev.fl.15.010183.002135.

Li, M., and C. Garrett, 1997: Mixed layer deepening due to Langmuir circulation. *J. Phys. Oceanogr.*, **27**, 121–132, doi:10.1175/1520-0485(1997)027<0121:MLDDTL>2.0.CO;2.

——, ——, and E. Skyllingstad, 2005: A regime diagram for classifying turbulent large eddies in the upper ocean. *Deep-Sea Res.*, **52**, 259–278, doi:10.1016/j.dsr.2004.09.004.

Li, Y., and M. Li, 2011: Effects of winds on stratification and circulation in a partially mixed estuary. *J. Geophys. Res.*, **116**, C12012, doi:10.1029/2010JC006893.

——, and ——, 2012: Wind-driven lateral circulation in a stratified estuary and its effects on the along-channel flow. *J. Geophys. Res.*, **117**, C09005, doi:10.1029/2011JC007829.

Lin, W., L. P. Sanford, and S. E. Suttles, 2002: Wave measurement and modeling in Chesapeake Bay. *Cont. Shelf Res.*, **22**, 2673–2686, doi:10.1016/S0278-4343(02)00120-6.

Longuet-Higgins, M. S., 1970: Longshore currents generated by obliquely incident sea waves: 1. *J. Geophys. Res.*, **75**, 6778–6789, doi:10.1029/JC075i033p06778.

——, and R. W. Stewart, 1960: Changes in the form of short gravity waves on long waves and tidal currents. *J. Fluid Mech.*, **8**, 565–583, doi:10.1017/S0022112060000803.

——, and ——, 1964: Radiation stresses in water waves; A physical discussion, with applications. *Deep-Sea Res. Oceanogr. Abstr.*, **11**, 529–562, doi:10.1016/0011-7471(64)90001-4.

Markfort, C. D., A. L. S. Perez, J. W. Thill, D. A. Jaster, F. Porte-Agel, and H. G. Stefan, 2010: Wind sheltering of a lake by a tree canopy or bluff topography. *Water Resour. Res.*, **46**, W03530, doi:10.1029/2009WR007759.

McWilliams, J. C., P. P. Sullivan, and C.-H. Moeng, 1997: Langmuir turbulence in the ocean. *J. Fluid Mech.*, **334**, 1–30, doi:10.1017/S0022112096004375.

——, E. Huckle, J. H. Liang, and P. P. Sullivan, 2012: The wavy Ekman layer: Langmuir circulations, breaking waves, and Reynolds stress. *J. Phys. Oceanogr.*, **42**, 1793–1816, doi:10.1175/JPO-D-12-07.1.

Melville, W. K., 1996: The role of surface-wave breaking in the air-sea interaction. *Annu. Rev. Fluid Mech.*, **28**, 279–321, doi:10.1146/annurev.fl.28.010196.001431.

——, F. Veron, and C. J. White, 2002: The velocity field under breaking waves: Coherent structures and turbulence. *J. Fluid Mech.*, **454**, 203–233, doi:10.1017/S0022112001007078.

Mitsuyasu, H., 1985: A note on the momentum transfer from wind to waves. *J. Geophys. Res.*, **90**, 3343–3345, doi:10.1029/JC090iC02p03343.

Monismith, S. G., and D. A. Fong, 2004: A note on the potential transport of scalars and organisms by surface waves. *Limnol. Oceanogr.*, **49**, 1214–1217, doi:10.4319/lo.2004.49.4.1214.

Oost, W. A., G. J. Komen, C. M. J. Jacobs, and C. van Oort, 2002: New evidence for a relation between wind stress and wave age from measurements during ASGAMAGE. *Bound.-Layer Meteor.*, **103**, 409–438, doi:10.1023/A:1014913624535.

Panofsky, H. A., and J. A. Dutton, 1984: *Atmospheric Turbulence*. Wiley, 397pp.

Phillips, O. M., 1985: Spectral and statistical properties of the equilibrium range in wind generated gravity waves. *J. Fluid Mech.*, **156**, 505–531, doi:10.1017/S0022112085002221.

Plueddemann, A. J., and R. A. Weller, 1999: Structure and evolution of the oceanic surface boundary layer during the Surface Waves Processes Program. *J. Mar. Syst.*, **21**, 85–102, doi:10.1016/S0924-7963(99)00007-X.

Potter, H., C. O. Collins, W. M. Drennan, and H. C. Graber, 2015: Observations of wind stress direction during Typhoon Chaba (2010). *Geophys. Res. Lett.*, **42**, 9898–9905, doi:10.1002/2015GL065173.

Rabe, T. J., T. Kukulka, I. Ginnis, T. Hara, B. G. Reichl, E. A. D'Asaro, R. R. Harcourt, and P. P. Sullivan, 2015: Langmuir turbulence under Hurricane Gustav (2008). *J. Phys. Oceanogr.*, **45**, 657–677, doi:10.1175/JPO-D-14-0030.1.

Rapp, R. J., and W. K. Melville, 1990: Laboratory measurements of deep-water breaking waves. *Philos. Trans. Roy. Soc. London*, **A331**, 735–800, doi:10.1098/rsta.1990.0098.

Rieder, K. F., J. A. Smith, and R. A. Weller, 1994: Observed directional characteristics of the wind, wind stress, and surface waves on the open ocean. *J. Geophys. Res.*, **99**, 22 589–22 596, doi:10.1029/94JC02215.

Sanford, L. P., and W. C. Boicourt, 1990: Wind-forced salt intrusion into a tributary estuary. *J. Geophys. Res.*, **95**, 13 357–13 371, doi:10.1029/JC095iC08p13357.

Schwendeman, M., J. Thomson, and J. R. Gemmrich, 2014: Wave breaking dissipation in a young wind sea. *J. Phys. Oceanogr.*, **44**, 104–127, doi:10.1175/JPO-D-12-0237.1.

Scully, M. E., 2010a: Wind modulation of dissolved oxygen in Chesapeake Bay. *Estuaries Coasts*, **33**, 1164–1175, doi:10.1007/s12237-010-9319-9.

——, 2010b: The importance of climate variability to wind-driven modulation of hypoxia in Chesapeake Bay. *J. Phys. Oceanogr.*, **40**, 1435–1440, doi:10.1175/2010JPO4321.1.

——, 2013: Physical controls on hypoxia in Chesapeake Bay: A numerical modeling study. *J. Geophys. Res. Oceans*, **118**, 1239–1256, doi:10.1002/jgrc.20138.

——, A. W. Fisher, S. E. Suttles, L. P. Sanford, and W. C. Boicourt, 2015: Characterization and modulation of Langmuir circulation in Chesapeake Bay. *J. Phys. Oceanogr.*, **45**, 2621–2639, doi:10.1175/JPO-D-14-0239.1.

——, J. H. Trowbridge, and A. W. Fisher, 2016: Observations of the transfer of energy and momentum to the oceanic surface boundary layer beneath breaking waves. *J. Phys. Oceanogr.*, **46**, 1823–1837, doi:10.1175/JPO-D-15-0165.1.

Smith, S. D., and Coauthors, 1992: Sea surface wind stress and drag coefficients: The HEXOS results. *Bound.-Layer Meteor.*, **60**, 109–142, doi:10.1007/BF00122064.

Sullivan, P. P., J. C. McWilliams, and W. K. Melville, 2004: The oceanic boundary layer driven by wave breaking with stochastic variability. I: Direct numerical simulations. *J. Fluid Mech.*, **507**, 143–174, doi:10.1017/S0022112004008882.

——, ——, and ——, 2007: Surface gravity wave effects in the oceanic boundary layer: Large-eddy simulation with vortex force and stochastic breakers. *J. Fluid Mech.*, **593**, 405–452, doi:10.1017/S002211200700897X.

——, L. Romero, J. C. McWilliams, and W. K. Melville, 2012: Transient evolution of Langmuir turbulence in ocean boundary layers driven by hurricane winds and waves. *J. Phys. Oceanogr.*, **42**, 1959–1980, doi:10.1175/JPO-D-12-025.1.

Tennekes, H., and J. L. Lumley, 1972: *A First Course in Turbulence*. MIT Press, 300 pp.

Terray, E. A., M. A. Donelan, Y. C. Agrawal, W. M. Drennan, K. K. Kahma, A. J. Williams III, P. A. Hwang, and S. A. Kitaigorodskii, 1996: Estimates of kinetic energy dissipation under breaking waves. *J. Phys. Oceanogr.*, **26**, 792–807, doi:10.1175/1520-0485(1996)026<0792:EOKEDU>2.0.CO;2.

Thomson, J., A. Jessup, and J. Gemmrich, 2009: Energy dissipation and the spectral distribution of whitecaps. *Geophys. Res. Lett.*, **36**, L11601, doi:10.1029/2009GL038201.

——, E. A. D' Asaro, M. F. Cronin, W. E. Rogers, R. R. Harcourt, and A. Shcherbina, 2013: Waves and the equilibrium range at Ocean Weather Station P. *J. Geophys. Res. Oceans*, **118**, 5951–5962, doi:10.1002/2013JC008837.

Van Roekel, L. P., B. Fox-Kemper, P. P. Sullivan, P. E. Hamlington, and S. R. Haney, 2012: The form and orientation of Langmuir cells for misaligned winds and waves. *J. Geophys. Res.*, **117**, C05001, doi:10.1029/2011JC007516.

Wilczak, J., S. Oncley, and S. Stage, 2001: Sonic anemometer tilt correction algorithms. *Bound.-Layer Meteor.*, **99**, 127–150, doi:10.1023/A:1018966204465.

Zijlema, M., G. Ph. van Vledder, and L. H. Holthuijsen, 2012: Bottom friction and wind drag for spectral wave models. *Coastal Eng.*, **65**, 19–26, doi:10.1016/j.coastaleng.2012.03.002.